Anticrossing spectrometry with synchrotron light

M. Žitnik,[1,2] K. Bučar,[1] R. Richter,[3] M. Coreno,[3] M. Kavčič,[1] Ž. Barba,[1] and A. Mihelič[1]

[1]*Jožef Stefan Institute, Jamova cesta 39, 1000 Ljubljana, Slovenia*
[2]*Faculty of Mathematics and Physics, University of Ljubljana, Jadranska 19, 1000 Ljubljana, Slovenia*
[3]*Elettra Sincrotrone Trieste, Strada Statale 14, km 163, 34149 Basovizza, Trieste, Italy*

(Received 11 January 2017; published 17 July 2017)

The anticrossing structure of the $1s7l$ manifold of the helium atom in combined dc electric and magnetic fields is studied using a broadband photoexcitation with synchrotron light. The anticrossing signal is provided by the yield of atoms in the metastable $1s2s$ states to which the $1s7l$ states cascade. The mapping resolution depends solely on the homogeneity of the two fields in the target region, which is formed by the intersection of the synchrotron beam and the helium atom beam. The measured positions, as well as anticrossing intensities and widths, measured in the region of 1–1.5 kV/cm and 0–10 mT are in excellent agreement with the results of our extended theoretical simulations based on highly accurate zero-field wave functions. By centering the photoexcitation window to 65.110 and 65.130 eV, the same technique is applied to look for the anticrossings in the vicinity of the $7^+ \, {}^1P_1^o - 7d \, {}^3D_1^o$ and $7d \, {}^1P_1^o - 8^- \, {}^1P_1^o$ pairs of doubly excited states, respectively.

I. INTRODUCTION

Anticrossings are formed when energy levels are prevented from crossing due to a small interaction between the corresponding states. The interaction results in a strong mixing of nearby states and the resulting energy levels appear to "repel" each other. The levels may be driven to the crossing by an internal process, such as molecular dissociation, or alternatively by tuning the strength of an external electric or magnetic field.

Anticrossing spectrometry (AS) studies weak interactions between the levels by measuring a signal that may change in the vicinity of the anticrossing. For example, to study spin-orbit (SO) interaction, the levels may be driven by a dc magnetic field and the state mixing in the anticrossing region is reflected by the intensity of the fluorescence emission signal to a "constant" lower state [1]. One can study anticrossings in the electronic ground-state manifold [2]; however, for AS, the higher-lying manifolds are mostly of interest due to the rich structure of levels coupled by fine and hyperfine interactions. For alkali-metal atoms, the energies of singly excited states (SESs) are low enough to be selectively excited from the ground state by a tunable laser light [3]. Other atoms are usually excited nonselectively, e.g., by charge exchange collisions of target ion beams with the gas [4] or by inelastic electron collisions with the gaseous target [1]. Lack of a precise knowledge about the initially excited populations and the possibility of an indirect population of anticrossings by radiative cascades make an accurate modeling of the AS signal very challenging.

A more controlled two-photon excitation scheme was set up to study the interaction of high-lying ns states in potassium with the rest of the Stark driven manifold [5]. Anticrossing symmetry was performed by observing an ion signal collected upon pulsed field ionization of potassium Rydberg states populated from an anticrossing by absorption of IR photons. These were provided by 300 K blackbody radiation to remove the laser broadening contribution to an overall AS resolution depending only on homogeneity of the driving dc electric field. Recently, we reported the AS results obtained by an inverse scheme: A broadband synchrotron light was used to selectively excite the SES manifold of He with $n = 5$–9 and the yield of atoms in metastable states (MY) was measured as a function of a dc electric-field strength [6]. The experiment clearly demonstrated that selected anticrossings of lower-lying SES manifolds reappear due to the cascade decay when the photoexcitation window was tuned to the SES manifold with higher n.

In this paper the selective photoexcitation technique is extended by observation of anticrossings activated when the $n = 7$ SES manifold is populated only indirectly, by fluorescence decay of the $n = 7$ manifold of helium doubly excited states (DESs) at 65.1-eV photon energy. As shown below, the corresponding AS signal modulation exhibits only 0.2% intensity compared to the direct excitation case and could not be retrieved without a selective photoexcitation of the DESs and use of the efficient MY detection scheme. Compared to [6], the AS technique adds a scan over a dc magnetic field $\boldsymbol{B}$ perpendicular to the electric field $\boldsymbol{F}$. Such a combination of fields breaks the axial symmetry of the experiment, which leads to a larger number of anticrossings. In present approach the AS resolution is limited only by spatial inhomogeneity of external fields allowing detection of weak interactions with narrow anticrossings. Precisely measured positions, anticrossing intensities, and widths of the $n = 7$ SES manifold are modeled by first calculating accurate eigenstates in nonzero F and B fields and then simulating ground-state excitation together with the cascade decay to the final metastable states. As shown below, in the studied case most of the AS signal behavior can be explained by a simpler model relying only on the field dependence of weights of pure LSJ states used as a basis for the description of atomic states.

Recently, a helium lamp was employed to purify the MY signal [7], essentially by quenching its singlet component (SMY) by photoexcitation to the $1s2p$ state decaying to the ground state with 99.9% probability [8]. The results indicate that a substantial contribution to the observed MY in the zero field is due to the SO coupling of SESs involved in the radiative cascade that actually started by photoexcitation of

DESs. Indeed, it is known that for $1snL\ ^{1,3}L_J$ states with the total orbital angular momentum $L \geqslant 3$, the SO mixing is nearly complete. It is therefore important to isolate the effects due to the SO coupling of DESs alone, which are much less studied than the SO coupling of SESs [9]. Below we look for DES anticrossings by comparing the well understood AS results obtained by a direct photoexcitation of the $n = 7$ SES manifold with the results obtained by an indirect excitation of the same manifold populated by fluorescence decay of the photoexcited $n = 7$ DES manifold. Due to the dipole selection rules, the latter case activates different SES anticrossings, mainly those with a considerable $^1D_2^e$ multiplet component [10]. Apart from this change, any deviations of the measured AS are expected to signal genuine DES anticrossings.

The main result of this and of our previous paper [6] is that the presented theory can be employed with confidence to simulate the entire anticrossing signal of He singly excited states ($n \leqslant 9$) with great accuracy when the signal is driven by a combination of dc electric (up to 10 kV/cm) and dc magnetic fields (up to 10 mT) and the yield of atoms in metastable states is observed. Together with selective photoexcitation provided by synchrotron light, this opens the possibility to study anticrossings in upper spectral regions inhabited by states that populate SES manifolds by radiative decay. The principle is demonstrated by analyzing the field dependence of the observed MY signal upon excitation of DESs by ~65-eV photons.

II. EXPERIMENT

In the past decade a relatively weak DES to SES radiative decay channel was exploited to observe the effects of SO mixing of DESs by detecting MY [11]. When SO coupling of SESs is vanishingly small, i.e., for $l \leqslant 2$, about 3% of radiative cascades starting from a singlet SES [8] pass by the $1s2s\ ^1S$ metastable state, which has a lifetime of 20 ms [12], and the rest promptly populate $1s^2\ ^1S$, the ground state of the atom. On the other hand, 100% of the cascades starting from a triplet SES end up in the $1s2s\ ^3S$ metastable state exhibiting a 8×10^3 s lifetime [13]. Because of such a large difference in the branching ratio, it is clear that detection of atoms in metastable states is a sensitive tool to mark any crossovers from the singlet to the triplet radiative decay channel caused, for example, by SO mixing, in either SES or DES manifolds. Also, MY can be detected with the low background signal: Good directionality of the supersonic atomic beam allows the MY detector to maintain good collection efficiency even when placed far away from the target.

Instead of observing MY as a function of photon excitation energy, the same phenomena may be employed to study anticrossings in the presence of moderate external fields: At a few kV/cm the field-induced mixing is still too weak to cause significant decay of metastable states before atoms reach the detector [6]. The observed MY variation therefore signals a redistribution of population of singlet and triplet metastable states due to changes of upper atomic states in the presence of external fields.

The magnetic field was generated by means of a small Helmholtz coil setup composed of three mutually perpendicular pairs of coils with 70 mm diameter. The primary coil pair
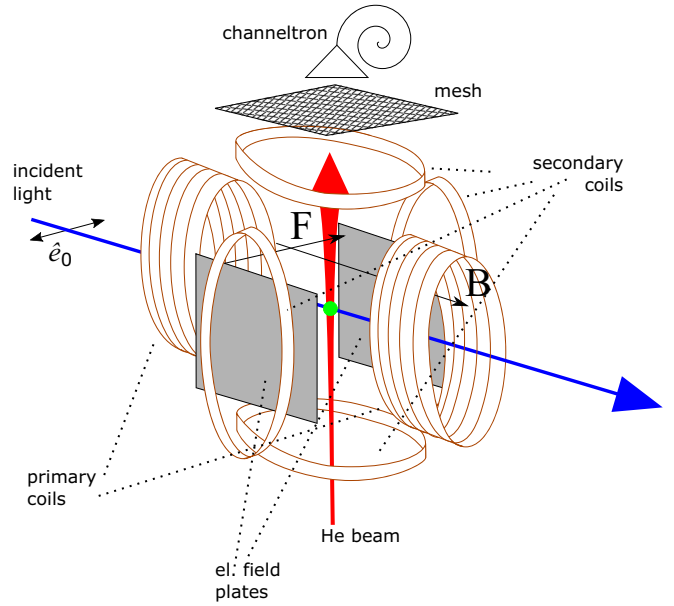

FIG. 1. Schematic of the experimental setup with the light beam and the supersonic atomic beam intersecting in the center of electric-field plates and magnetic-field coils.

had altogether 140 turns of wire and was set with its axis along the photon beam direction (Fig. 1). The current in the primary coil went up to 7 A, resulting in a magnetic-field strength of 10 mT in the target region. A dc electric field at the crossing of the light beam and the supersonic gas beam was generated by setting the voltage on two parallel $130 \times 40\ mm^2$ metal plates separated by 16 mm. The whole arrangement was water cooled in order to maintain its temperature in the vacuum environment below 60 °C. The secondary coil pairs with 14 turns of wire each allowed for a compensation of the residual static magnetic field. However, it turned out that in the investigated field range a weak peak in the MY (see Fig. 5 below) persisted at all possible compensation settings, indicating its origin as due to the presence of a small ac magnetic field in the target region.

The experiment started by measuring MY without any static field present, using a few-meV narrow photon probe to locate SES excitation energies. The MY detector was a channeltron with 20-mm-diam opening, configured for an ion detection and equipped with a mesh in front, set to a 300-V bias voltage to reject the ions. The detector was placed inline with the supersonic gas beam, 50 cm away from the beam skimmer and 40 cm away from the interaction region. After the initial setting the beamline slits were opened to 50 μm and 200 μm, respectively, to broaden the photon beam spectrum to a box-type profile with ~45 meV width centered at the excitation energy of the $1s7p\ ^1P$ state at 24.304 eV [14]. As shown by the photon energy scan in Fig. 2, such a setting exhibited a quite uniform spectral density distribution in the whole energy interval occupied by the $n = 7$ manifold (including field-induced broadening) and avoided photoexcitation of the neighboring manifolds. To acquire a MY (F, B) map of the selected manifold, electric current in the primary coil was changed in 0.5-A steps within the 0–7 A range using a computer-controlled digital-to-analog converter
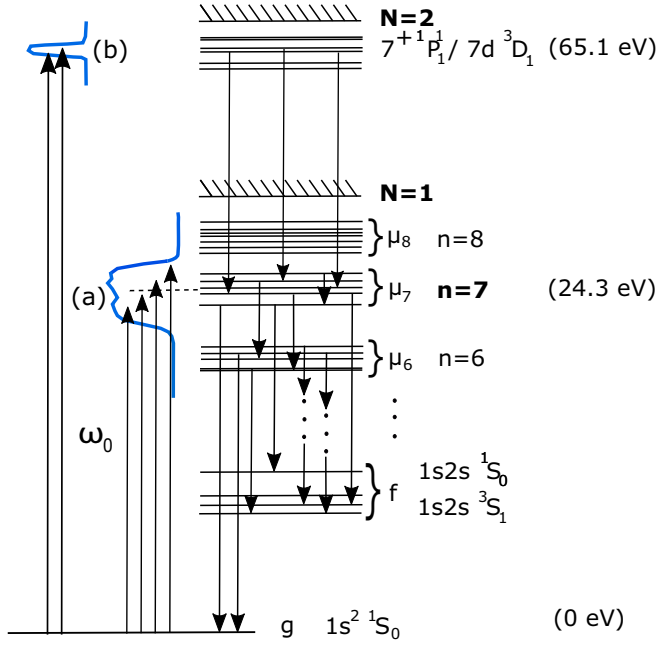
FIG. 2. Emission cascades in the He atom started by broadband photoexcitation of (a) the $n = 7$ SES manifold and (b) the $7^+ \, ^1P_1$ and $7d \, ^3D_1$ DESs below the $N = 2$ ionization threshold.

Marconi connected to the Xantrex XKW60-18 power supply. At each current setting a scan of the electric-field strength was performed using a pair of NHQ 206L power supplies to change the negative voltage on one of the field plates in 2-V steps with the other plate voltage fixed to 1500 V. At each (F, B) point the MY counts were acquired for 5 s, resulting in couple of hours long F scans where the additional time delays were inserted to stabilize the voltage settings. In the case of DES photoexcitation, the accumulation time was increased to 30 s per point and the electric-field strength scans were executed only for two settings of the magnetic field: zero and 7 mT.

III. THEORY

The calculation of the metastable atom yield upon box-type photoexcitation is described in detail in Ref. [6]. Here we only give a brief outline of the calculation, expanded by adding an external magnetic-field interaction to the atomic Hamiltonian. The number of atoms in the metastable states (f) is described by

$$N = \sum_f \sum_{s=1}^{\infty} \sum_{\mu_1,\dots,\mu_s} \frac{\Gamma_{f,\mu_s}}{\Gamma_{\mu_s}} \left(\prod_{j=1}^{s-1} \frac{\Gamma_{\mu_{j+1},\mu_j}}{\Gamma_{\mu_j}} \right) N_{\mu_1}^0, \qquad (1)$$

where s denotes the number of emission steps. The summation $\mu_1, \dots, \mu_s$ runs over all accessible states but the metastable states and the ground state. The partial and the total decay widths have been denoted by $\Gamma_{\zeta,\eta} \equiv \Gamma_{\zeta \leftarrow \eta}$ and Γ_η ($\zeta, \eta = \mu_1, \dots, \mu_s, f$), respectively. The number of atoms in state $|\mu_1\rangle$ after irradiation of the ensemble of ground-state atoms with the synchrotron beam has been denoted by $N_{\mu_1}^0$. The metastable atom yields reported here are normalized so that the total
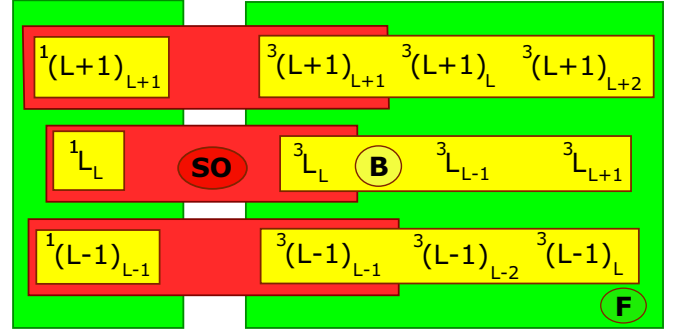

FIG. 3. Multiplet coupling due to V_{so} (SO), dc electric-field (F), and magnetic-field (B) interaction.

number of excited atoms is equal to unity:

$$\sum_{\mu_1} N_{\mu_1}^0 = 1. \qquad (2)$$

The partial and total decay widths have been calculated using the eigenfunctions and eigenenergies of the total Hamiltonian operator,

$$H = H_0 + H_F + H_B. \qquad (3)$$

Here $H_0 = H_{nr} + V_{so}$ describes the free atom, where H_{nr} represents a nonrelativistic (electrostatic) interaction and V_{so} includes relativistic and QED corrections. The interaction with the external electric field $\boldsymbol{F}$ is described by $H_F = \boldsymbol{F} \cdot (\boldsymbol{r}_1 + \boldsymbol{r}_2)$, where $\boldsymbol{r}_1$ and $\boldsymbol{r}_2$ are the electron coordinates. The interaction with the external magnetic field $\boldsymbol{B}$ is given by $H_B = \frac{1}{2} \boldsymbol{B} \cdot (\boldsymbol{L} + g_s \boldsymbol{S})$, where $\boldsymbol{S}$ denotes the spin operator and g_s is the electron g factor. The effect of the diamagnetic term (proportional to B^2) is small and has been neglected in the present calculations.

Previously we developed codes that diagonalize the nonrelativistic Hamiltonian H_{nr} of helium atom to obtain highly accurate wave functions of SES multiplets $|\gamma L S J\rangle$ [15]. Below we briefly recall the selection rules for coupling the eigenstates by the V_{so} interaction and by static-field interactions in order to expose symmetries of the full H diagonalization problem (Fig. 3).

In the isolated atom the total angular momentum J and its projection M are conserved and the only nonzero matrix elements due to V_{so} interaction are between the singlet-triplet pairs of multiplets having the same γ, L, J, and M quantum numbers:

$$\langle \gamma' L 0 L M | V_{so} | \gamma L 1 L M \rangle = \frac{E_{\gamma' L 0} - E_{\gamma L 1}}{2} \tan 2\theta_{\gamma' L 0, \gamma L 1}.$$

Each matrix element is conveniently expressed by the singlet-triplet energy difference and mixing angle $\theta (0 \leqslant \theta < \pi/4)$. The latter was accurately calculated in the past [16] by diagonalizing H_0 in the $|\gamma L S J\rangle$ basis.

The Stark interaction obviously conserves the total spin S. When the quantization axis is along $\boldsymbol{F}$ the only nonzero matrix

elements

$$
\langle \gamma'L'SJ'M'|H_F|\gamma LSJM \rangle
$$
$$
= F(-1)^{J'+L+S+J-M}\sqrt{[J,J']}\langle \gamma'L'S||\boldsymbol{r}_1+\boldsymbol{r}_2||\gamma LS\rangle
$$
$$
\times \begin{pmatrix} J' & 1 & J \\ -M & 0 & M \end{pmatrix} \begin{Bmatrix} L' & S & J' \\ J & 1 & L \end{Bmatrix} \tag{4}
$$

are those with $L' = L \pm 1$ because the state's parity must change to obtain a nonzero reduced matrix element $\langle ||\rangle$. The notation $[X,Y,\ldots]$ means $(2X+1)(2Y+1)\cdots$.

If the quantization axis is chosen along $\boldsymbol{B}$, the nonzero Zeeman matrix elements are given by

$$
\langle \gamma LSJ'M|H_B|\gamma LSJM \rangle
$$
$$
= \frac{B}{2}\Bigg[M\delta_{J',J} - (g_s-1)(-1)^{L+S+M}\sqrt{[J,J',S]}S(S+1)
$$
$$
\times \begin{pmatrix} J & 1 & J' \\ -M & 0 & M \end{pmatrix} \begin{Bmatrix} J' & 1 & J \\ S & L & S \end{Bmatrix} \Bigg], \tag{5}
$$

and the magnetic field couples $J' = J, J \pm 1$ multiplets with the same quantum numbers L, S, and M. However, in our experimental geometry it is more convenient to set the quantization axis perpendicular to $\boldsymbol{B}$ (and parallel to $\boldsymbol{F}$ and $\hat{e}_0$). In that case the magnetic field couples states with $M' = M \pm 1$.

Let us now examine a pair of interacting states whose energy levels form an anticrossing at $F = F_c$. The eigenstates of $H(F_c,B)$ are denoted by $|a\rangle$ and $|b\rangle$ and the corresponding eigenenergies by E_a and E_b. We assume that the magnitude of the magnetic field is held constant. The behavior close to F_c is approximately described by the following matrix [6]:

$$
\mathsf{H} = \begin{pmatrix} E_a & v\delta F \\ v^*\delta F & E_b \end{pmatrix} \tag{6}
$$

where $\delta F = F - F_c$ and $v = \langle a|\hat{e}_0 \cdot (\boldsymbol{r}_1 + \boldsymbol{r}_2)|b\rangle$ describes the coupling by the field. The eigenenergies close to F_c are written as

$$
E_{1,2} = \frac{E_a + E_b}{2} \mp |v|\sqrt{\delta F^2 + \gamma^2/4}, \tag{7}
$$

where $\gamma = |E_a - E_b|/|v|$ denotes the width of the region of the electric-field strength where the anticrossing occurs (Fig. 4). Out of the crossing the eigenstates are given by

$$
\begin{pmatrix} \Phi_1 \\ \Phi_2 \end{pmatrix} = \begin{pmatrix} \cos\varphi & \sin\varphi \\ -\sin\varphi & \cos\varphi \end{pmatrix} \begin{pmatrix} a \\ b \end{pmatrix}, \tag{8}
$$

where $\tan 2\varphi = 2|v|\delta F/(E_a - E_b)$ and the mixing angle φ is limited to the interval $[-\pi/4,\pi/4]$. When $\delta F \to -\infty$ (and consequently $\varphi = -\pi/4$), the $F \ll F_c$ asymptotic states are obtained:

$$
\Phi_{1,2}(-\pi/4) = |\eta_{1,2}\rangle = \frac{1}{\sqrt{2}}(|a\rangle \mp |b\rangle). \tag{9}
$$

To obtain the asymptotic states $|\eta'_{1,2}\rangle$ of two levels on the other side of the crossing (at $\varphi = \pi/4$), the symmetric and antisymmetric combination of states in (9) are exchanged, as well as the $|a\rangle$ and $|b\rangle$ states within each combination. Alternatively, by inverting (8) one sees that eigenstates at the
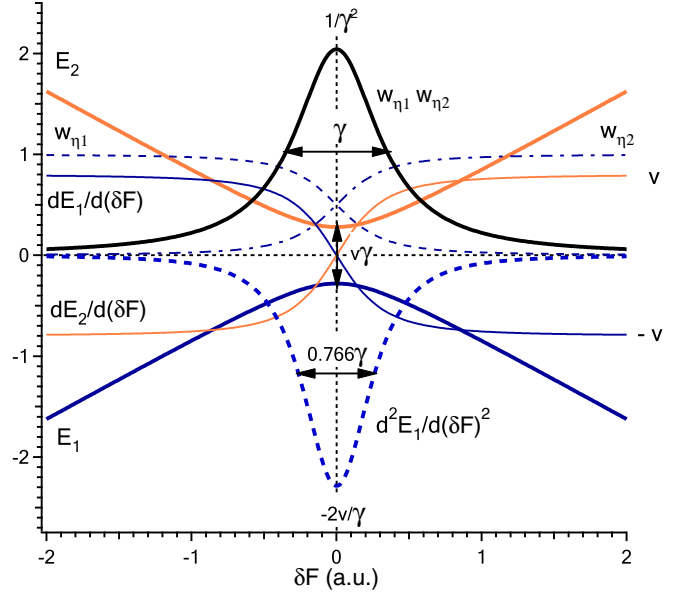

FIG. 4. Energy levels E_1 and E_2 [Eq. (7)] and the first [$dE_1/d\delta F$ and $dE_2/d\delta F$, Eq. (10)] and second [$dE_1^2/d\delta F^2$, Eq. (13)] derivatives in a.u. depending on the electric-field detuning δF. Also presented is the field dependence of weights of asymptotic states [w_{η_1} and w_{η_2}, Eq. (11)] and of their product $w_{\eta_1}w_{\eta_2}$ [Eq. (12)] in the vicinity of the anticrossing for $E_a + E_b = 0$ a.u., $\gamma = 0.7$ a.u., and $v = 0.8$ a.u.

crossing ($\delta F = 0$) are expressed as a half-half mixture of the asymptotic states $|\eta_{1,2}\rangle$.

Any anticrossing can be conveniently located in the $E(F)$ diagram by examining derivatives of the eigenenergies with respect to the field strength. In an isolated two-level system the derivatives are given by

$$
\frac{\partial E_{1,2}}{\partial(\delta F)} = \mp|v|\,\delta F/\sqrt{\delta F^2 + \gamma^2/4}. \tag{10}
$$

They form a pair of complementary step-shaped functions whose values change over an interval of the order of γ, centered at $\delta F = 0$ (Fig. 4). It is interesting to note that weights (squared modulus of the corresponding mixing coefficients) of the asymptotic $|\eta_{1,2}\rangle$ eigenstates in the $|\Phi_1\rangle$ eigenfunction (8), namely, $w_{\eta_{1,2}} = (\cos\varphi \mp \sin\varphi)^2/2$, follow the same δF dependence as the gradients (10):

$$
w_{\eta_{1,2}}(\delta F) = (1/2)(1 \mp \delta F/\sqrt{\delta F^2 + \gamma^2/4}). \tag{11}
$$

For the $|\Phi_2\rangle$ eigenstate the same formula holds with the $\pm$ sign, i.e., the weights of asymptotic states are exchanged. While gradients jump between $\pm v$, the weights jump between 1 and 0 when δF changes through the crossing (Fig. 4).

When one asymptotic eigenstate of the interacting level pair is coupled only to the initial state and the other only to the final state, the population transfer from the initial to the final state is zero out of the crossing and is the largest exactly at the crossing ($F = F_c$). While in general the population transfer can assume different types of δF dependence [6,17,18], we are dealing here with exactly the above generic situation: By photon absorption the singlet asymptotic state gets populated, photon emission of the triplet asymptotic state leads to the triplet metastable yield (TMY), and there is an enhanced

interaction of the two asymptotic states at the crossing due to the V_{so} interaction. The population transfer is then proportional to the product of weights $w_{\eta_1} w_{\eta_2}$, which, according to (11), has the form of a Lorentzian with FWMH equal to γ (Fig. 4):

$$\text{TMY} \propto (1/4)/(\delta F^2 + \gamma^2/4). \tag{12}$$

The calculated TMY signal consists of contributions due to many different cascade paths and is given by the sum of Lorentzian peaks (discussed below). The Lorentzians have different widths and intensities and they are centered at field coordinates of the avoided level crossings.

It is worth mentioning that both the width γ and the field strength F_c at which the anticrossing is formed are directly measured by the present experimental setup. However, to obtain the coupling strength $|v|$ of a given crossing, one would need to divide the calculated minimum level separation by the measured width. Alternatively, $|v|$ is directly exposed in $\partial E/\partial F$, equaling one-half of the derivative jump across the crossing (10), the quantity that can be relatively easily retrieved from the calculated Stark-Zeeman energy map. However, as shown below, the coupling strength $|v|$ is not directly associated with the measured TMY signal of the corresponding crossing because the magnitude of the signal depends also on its activation, i.e., on the probability that the interacting pair of levels actually takes part in the population transfer towards final states.

IV. RESULTS AND DISCUSSION

In Fig. 5 the measured data set is compared to the result of calculations. There is good overall agreement between the two when the experimental electric- and magnetic-field scales are calibrated to match the calculated peak positions: The electric-field strength was found to be proportional to the potential difference of field plates according to $F = \triangle U \times 0.613\,\text{cm}^{-1}$ (where F is in units of kV/cm and $\triangle U$ is in kV) and the magnetic-field density is proportional to the coil current $B = I \times 1.44\,\text{mT/A}$ (where B is in mT and I in A).

As our simulation shows, the sole variation of B up to 10 mT does not induce peaks in the MY for SES manifolds with moderate n: Sharp peaks appear only when a properly selected electric field is present in the target region. This is because the magnetic interaction is relatively weak and energy levels need to be brought closer to each other by a dc Stark effect to form anticrossings that can transfer extra population to the metastable states. On the other hand, the comparison with experimental data taken at $I = 0$ A shows that a sharp peak observed at 1.142 kV/cm must be attributed to the presence of a nonzero magnetic field in the target region because the peak clearly appears in the model as soon as B deviates from zero. The persistence of this peak, as well as other observed small differences with the calculated $B = 0$ spectrum (discussed below), could be explained by the presence of a small ac magnetic field that cannot be compensated by the static Helmholtz coil arrangement. Still, as shown by the comparison in Fig. 5, most of the observed signal modulation at nonzero B is due to the controlled presence of a dc magnetic field.
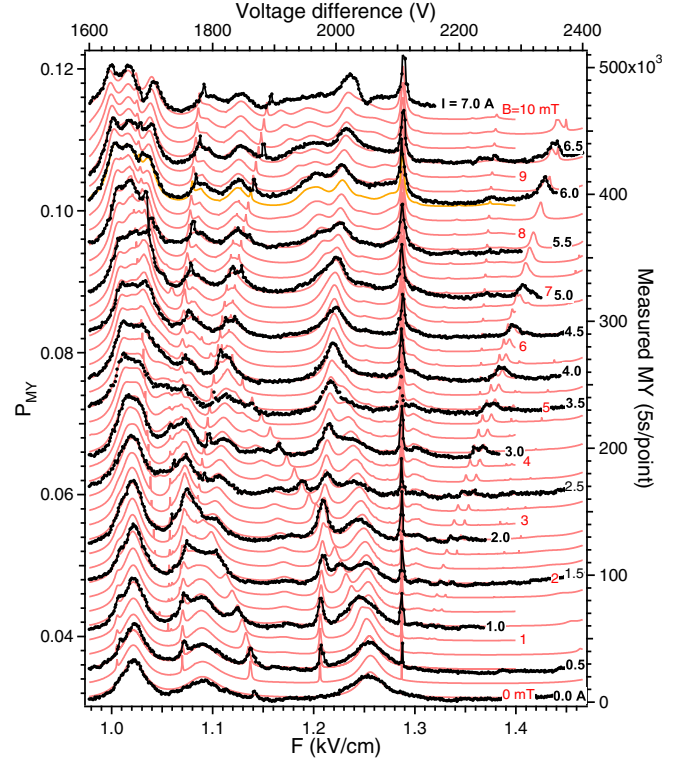

FIG. 5. Measured (black dots) MY dependence on the dc electric field F for different values of the magnetic field B. For a clear comparison the calculated probabilities P_{MY} to populate metastable states [pink (gray) curves] are offset by 0.002 for each 0.25-mT increase of B. Measured MY trends are denoted by the coil current and have an offset according to the magnetic-field calibration.

A. The $B = 0$ case

We continue with the analysis of the $I = 0$ A spectrum. Owing to the good agreement with the measured data, we can rely on simulations to split the channeltron signal into undiscriminated fractions: As a function of F the signal consists of a rather constant $\sim$50 kHz count rate pertaining to the SMY signal and the multichannel plate background, on top of which there is a $\sim$10% TMY signal modulation. Whenever F drives a pair of levels through the anticrossing, the peak in TMY signal is observed. As shown in Fig. 6(a), there is a large number of closely lying energy levels in the studied range of F, possibly forming many anticrossings. Altogether there are 196 states in the $n = 7$ manifold, composed of $^1S_0$, $^3S_1$, $^1P_1$, $^3P_{0,1,2}$, $^1D_2$, $^3D_{1,2,3}$, $^1F_3$, $^3F_{2,3,4}$ $^1G_4$, $^3G_{3,4,5}$, $^1H_5$, $^3H_{4,5,6}$, $^1I_6$, and $^3I_{5,6,7}$ multiplets. When $B = 0$, the projection of the total angular momentum on the direction of F is conserved and only multiplets with the same value of M are mixed by the field. As the photon beam is linearly polarized and parallel to F (and to the quantization axis), only the $M = 0$ submanifold of 26 states is accessible for photoexcitation. More precisely, only the states in this submanifold can mix with the $^1P_1(M = 0)$ multiplet, which exclusively has a nonzero dipole matrix element with the $1s^2\,{}^1S_0$ He ground state.

The positions of anticrossings are uncovered by plotting derivatives $\partial E/\partial F$ as a function of F [Fig. 6(b)]. At the crossing the slope of the derivative is the steepest and the derivatives of two interacting levels intersect, restoring
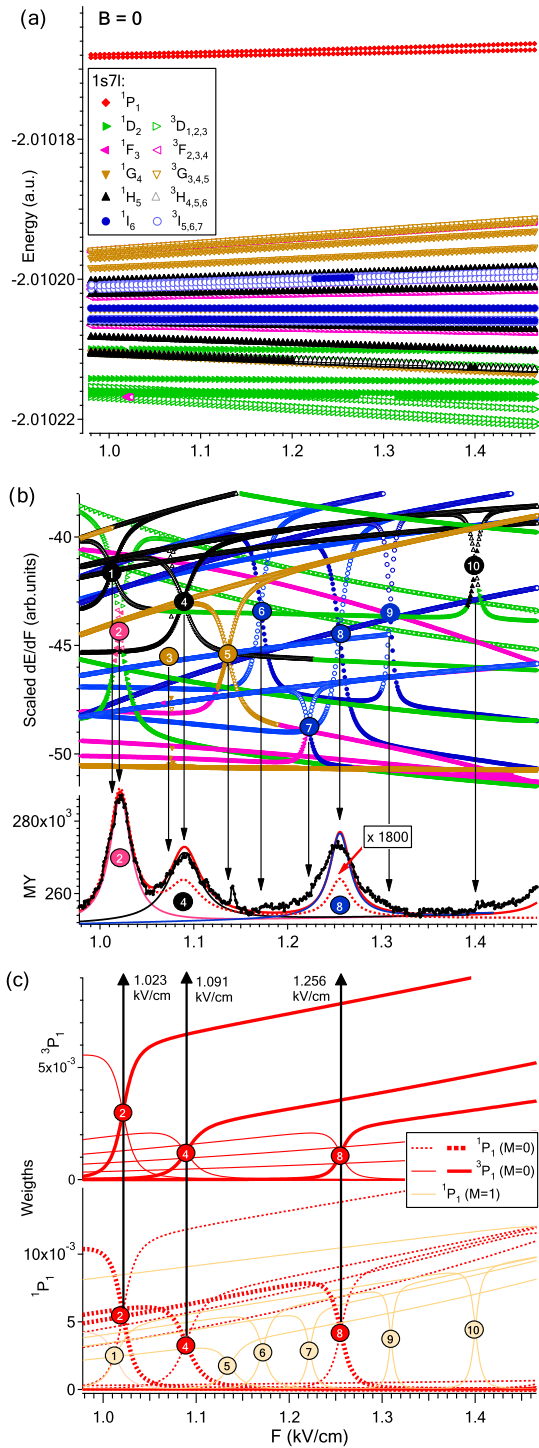
FIG. 6. (a) Energy levels of the $n = 7$ manifold as a function of F at $B = 0$ showing also the parent multiplet type. (b) Scaled level gradients uncover positions of anticrossings. Experimental data are shown by black circles and three Lorentzians fitted to the calculated trend by solid lines. The one-step decay contribution is given by the dotted line. (c) The F dependence of ^1P and ^3P weights for the 26 photoexcited levels with $M = 0$. Bold lines denote weights for levels that form crossings with the largest observed TMY signal.

(parent) multiplet component $|LSJM\rangle$. Inspecting the parent's weight in the quantum state, we are sure to follow the level if the weight change is correspondingly small when the field is changed for any small amount. Such a level tracing technique obviously requires very small steps in F when the field is close to a narrow crossing (γ is small) to prevent jumping on the avoided level. For a pair of energy levels, it turns out that their parent multiplets may or may not be exchanged after the anticrossing [Fig. 6(b)], because they are not true asymptotic eigenstates of energy levels. As shown below, the multiplet picture is still very convenient to understand the experimental results because the initial ground state and the observed metastable states are almost pure LSJ coupled states.

In Fig. 6(b) the derivatives are presented for levels without restricting their angular momentum projection M. One can see clearly that three prominent peaks in the observed MY signal are centered at the same value of F as the three $M = 0$ crossings marked by numbers 2, 4, and 8, giving also a good match for widths of the corresponding MY features. Inspecting parent multiplets in the vicinity of these crossings, one notes that numbers 4 and 8 are roughly associated with H and I orbital angular momenta, respectively, while the crossing number 2 deals with an orbital angular momentum F asymptotically turning into D. Figure 6(c) shows an F dependence of the $^1P_1(M = 0)$ weight for the 26 photoexcited energy levels and explains why these three crossings play the dominant role: The largest dipole-allowed weights are evidently associated with levels forming the crossings 2, 4, and 8 and allow for their substantial photoexcitation. As expected, due to the V_{so} interaction, exactly the same levels display also the largest $^3P_1(M = 0)$ multiplet weights, which substitute the $^1P_1$ weights on the other side of the crossing (Fig. 4).

By multiplying the F-dependent $^1P_1$ and $^3P_1$ weights for each level and summing the results over all levels one obtains a three-Lorentzian-peak structure that resembles the observed MY signal, albeit with much smaller intensity [Fig. 6(b)]. This is not surprising because such products describe only a direct $n\,^3P_1 \rightarrow 2\,^3S_1$ decay to the final triplet metastable state. This is a minor decay channel of photoexcited states because their $^3P_1$ weights are relatively small. The dominant contribution to MY is given by multistep cascade paths, as discussed in [6].

In Fig. 6(b) one can see that at $B = 0$ the calculated TMY is perfectly fitted by three Lorentzians. One also notes that the measured MY signal indicates some additional weak peaks in the studied range of F. Comparing Figs. 6(b) and 6(c), these can be associated with the anticrossings that involve energy levels with relatively large $^1P_1(M = 1)$ weight. Besides having some small residual magnetic field in the target (at $B = 0$ the photoexcitation to $M = 1$ states is forbidden), the origin of the observed weak features could be explained also by a dc electric field not being perfectly parallel to the polarization direction of the light.

B. The $B = 8.5$ mT case

Below we discuss the more complicated behavior of the MY signal collected at $B = 8.5$ mT. Looking at Fig. 7(a),

the low-F asymptotic slopes at higher F, albeit with level characters exchanged. To follow a given energy level with F we mark the corresponding quantum state by its largest
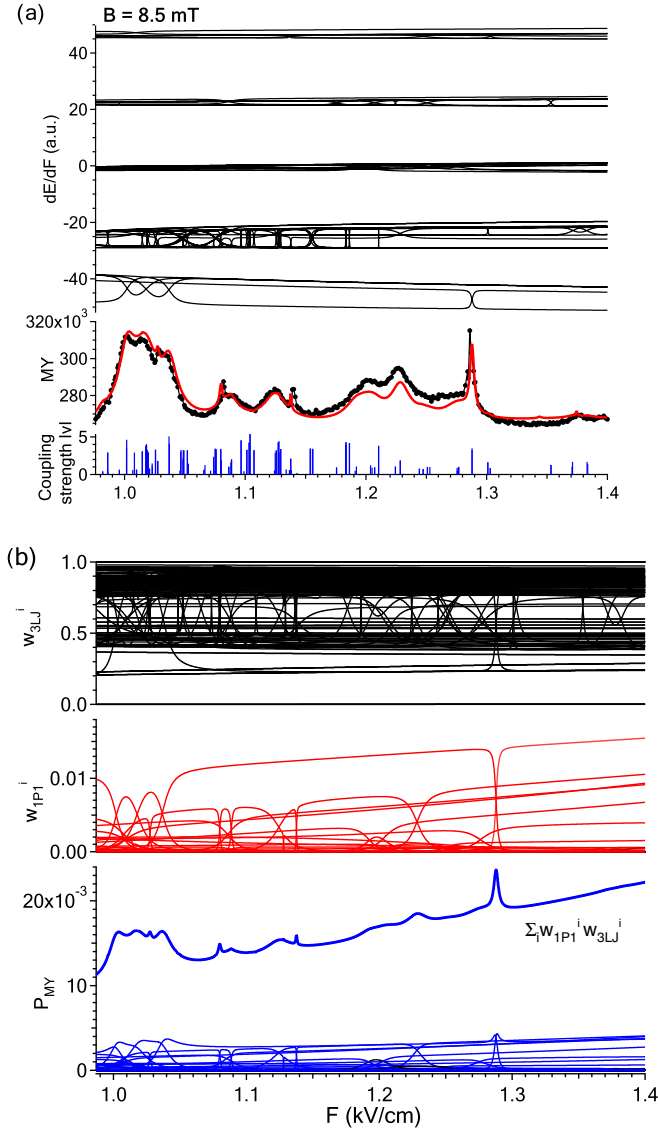
FIG. 7. (a) Gradients of energy levels in the $n = 7$ manifold at $B = 8.5$ mT (black curves). Measured MYs are shown by black points and calculated MYs by the red (gray) curve. The distribution of coupling strengths $|v|$ sticks to zero. (b) The $^1P(M = 0)$ multiplet weight (red curves) and the sum of ^3L_J multiplet weights (black curves) and their product $w^i_{1P1}w^i_{3LJ}$ (blue curves) for each level in the manifold. The sum of products for all levels is denoted by the thick blue line.

two things are noted immediately: (i) In a dense energy region the derivatives $\partial E/\partial F$ are organized into five groups corresponding roughly to the parent orbital angular momenta D to I [see also level slopes in Fig. 6(a)] and (ii) there are more anticrossings than in the $B = 0$ case [Fig. 6(b)], many of them very narrow. To obtain precise positions of anticrossings for a given energy level it is convenient to look for extremes of the second derivatives. In the case of the two-level system, they read

$$\frac{\partial^2 E_{1,2}}{\partial(\delta F)^2} = \pm v(\delta F^2/(\sqrt{\delta F^2 + \gamma^2/4})^3 - 1/\sqrt{\delta F^2 + \gamma^2/4}).$$

(13)

In Fig. 7(a) the coupling strengths $|v|$ are given by bar lengths at locations of the corresponding anticrossings. In fact, $2|v|$ measures level deflection in the $E(F)$ map due to the anticrossing with the other level experiencing deflection of the same magnitude but in the opposite sense. Instead of looking at one-half of the level gradient jump (10) across the anticrossing, the coupling strength was estimated locally to avoid the asymptotic region that is often obscured due to interaction with the other levels. First, the level's second derivative was obtained numerically from the F dependence of the level's gradient and then the integral over the crossing was estimated by multiplying the integrand's amplitude by the corresponding half-width at half maximum. For the locally valid two-level approximation (13), the product of the amplitude $2|v|/\gamma$ and HWHM given by $(\gamma/2)\sqrt{2^{2/3} - 1}$ is evidently proportional to the coupling strength (Fig. 4). One can see in Fig. 7(a) that while some anticrossing positions perfectly correspond to the observed peak positions, the coupling strength distribution bears a quite weak similarity to the observed MY.

Knowing the energy level map with all the corresponding quantum states, a good estimate of MY can be obtained by relying on the F dependence of the specific level's multiplet weights. The one-step approach, introduced above for the $B = 0$ case, is improved by replacing the $^3P_1(M = 0)$ weight by the sum w^i_{3LJ} of all ^3L_J weights entering the description of the quantum state of the ith level. In Fig. 7(b) both relevant types, the $^1P_1(M = 0)$ weight $w^i_{1P1}(M = 0)$ deciding the level's photoexcitation probability and the sum weight w^i_{3LJ} deciding the level's decay probability to triplet metastable states, are plotted. Because for $B \neq 0$ the axial symmetry is broken, M is not a good quantum number anymore and each of the 196 manifold states may hold a nonzero weight of the dipole-allowed multiplet. By multiplying F dependences of both weight types, namely, $w^i_{1P1}(M = 0)w^i_{3LJ}$, one obtains an estimate for the ith level contribution to TMY. When the sum of such estimates for all the levels, namely, $\sum_i w^i_{1P1}(M = 0)w^i_{3LJ}$, is compared to the observed MY [Fig. 7(b)], a very similar structure is displayed, except for a quasilinear rise of the sum, not reproduced by the experimental data. A similar procedure may be used to estimate the SMY part of the signal: In this case the $^1P_1(M = 0)$ weight is multiplied by the sum w^i_{1LJ} of all ^1L_J weights of the ith level, which is simply given by $w^i_{1LJ} = 1 - w^i_{3LJ}$. Before comparing to SMY from the full calculation, the sum $\sum_i w^i_{1P1}(M = 0)w^i_{1LJ}$ must be multiplied by an average probability $\nu = 0.03$ to reach the singlet metastable state (and not the ground state of the atom) by the radiative cascade process.

C. Effective branching ratio

The above MY estimate assumes that the partial decay rate of a singlet component of the manifold state (decaying into the singlet channel) relative to the partial decay rate of the triplet component (decaying into the triplet channel) is simply given by the ratio w^i_{1LJ}/w^i_{3LJ} of the total singlet to the total triplet weight of the ith level. Away from the anticrossings the level's singlet and triplet weights are changing slowly with F. Still, this variability may gradually cause significant changes of the relative singlet-to-triplet decay branching ratio because the lifetimes of pure $|LSJ\rangle$ states strongly depend
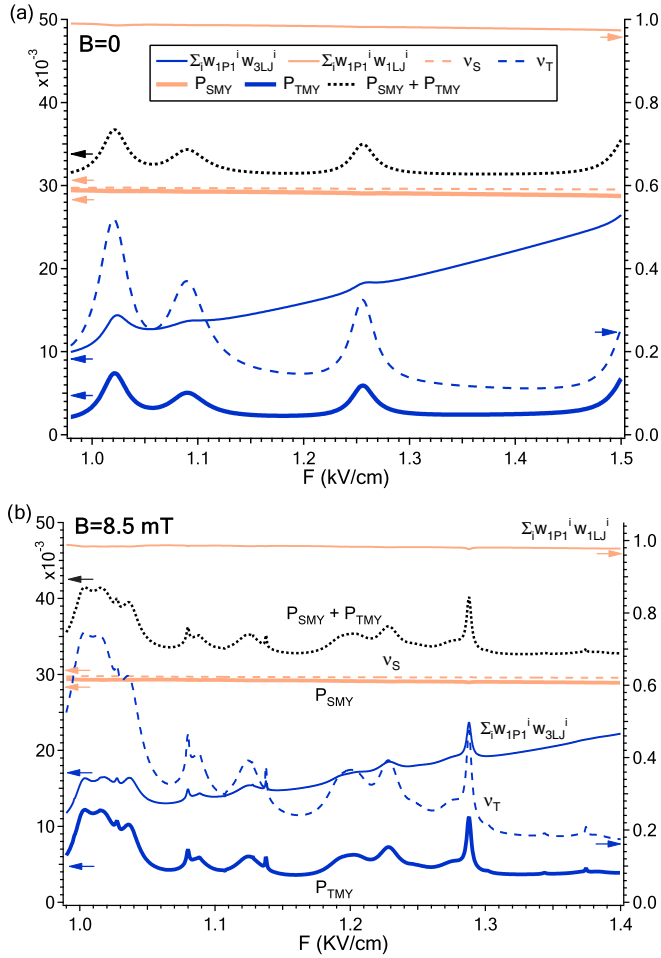
FIG. 8. Effective branching ratios ν_s and ν_t for the production of SMY and TMY, respectively, for a broadband photoexcitation of the $n = 7$ manifold of states when (a) $B = 0$ and (b) $B = 8.5$ mT. Arrows beside the graphs indicate the vertical scale to be used.

on the angular momenta (Table I). While the lifetimes of ^1L and ^3L states are practically equal for $L \geqslant 3$, they differ greatly for $L = 1$: The ^1P state decays much faster (20.6 ns) than the ^3P state (514 ns). A small admixture of the $^1P_1$ component therefore considerably speeds up decay into the singlet channel, practically compensating for the unphysical (not observed) rise of the triplet metastable yield, generated by the above simple model [Fig. 7(b)]. This effect can be formally examined by introducing an effective field-dependent branching ratio for decay of the singlet (triplet) component to the singlet (triplet) metastable state(s), simply by choosing the function that by multiplication restores the full calculation trend when the static value of 0.03(1) is taken for the branching. The thus obtained effective branching ratios for the triplet (ν_t) and for the singlet channel (ν_s) are shown in Fig. 8 for

$B = 0$ and 8.5 mT. While ν_s is fairly close to the static 0.03 value, ν_t is substantially less than 1 in the examined range of F. A quasilinear decrease of ν_t is explained by a gradually increasing admixture of the $^1P_1(M = 0)$ component in the predominantly higher angular momentum states, pulling its strength by means of F from a rather distant level with a practically pure $^1P_1$ character [see Fig. 6(c)]. Moreover, not only is ν_t a smoothly decreasing function of F but there is an extra contribution to the effective branching ratio across the anticrossings that favors TMY production. Technically, this enhancement is due to the neglect of the singlet-singlet and triplet-triplet interference terms contributing to the partial decay widths in the vicinity of the anticrossing where the asymptotic singlet (triplet) amplitudes of both levels are recombined to describe the two physical states. It therefore has no sense to push the simple model any further; for precise results one needs to work out the full calculation scheme.

D. Doubly excited states

Above we discussed MY emitted upon *direct* photoexcitation of the $n = 7$ SES manifold. In the past decade or so, several experimental and theoretical studies [10,11,19–23] have shown that the same SES manifold can be populated by a radiative decay of $n = 7$ DESs below the $N = 2$ ionization threshold. Although the fluorescence emission from DESs is quite weak due to the competing autoionization decay channel, it can be readily studied by observing atoms in metastable states. Still, the MY from photoexcited DESs is much smaller than MY from photoexcited SESs: For ground-state photoexcitation the total fluorescence cross section for $7^+ \, ^1P_1$ DESs (66.7 b eV [10]) is four orders of magnitude smaller than corresponding cross section for $7 \, ^1P_1$ SESs (59.3×10^4 b eV). To study indirectly populated SESs, longer accumulation times are therefore required and MY was measured as a function of F for two magnetic-field strengths only, 0 and 7 mT (Fig. 9). The photon energy was set to 65.11 eV with the beamline slits set to 30 μm and 200 μm, respectively, to obtain a 15-meV broadband photoexcitation profile covering $7^+ \, ^1P_1^o$ and $7d \, ^3D_1^o$ DESs [Fig. 8(a)]. The latter is predominantly a triplet state and gets photoexcited from the ground state due to SO interaction generating a small probability ($\kappa = 6 \times 10^{-4}$) to mix with the neighboring dipole-allowed $7^+ \, ^1P_1^o$ state [24]. For the $7d \, ^3D_1^o$ DES the autoionization is forbidden and it was shown previously that it decays almost exclusively to the $7 \, ^3D_{1,2}$ SES [24]. On the other hand, the $7^+ \, ^1P_1^o$ multiplet does autoionize with 99% probability, leaving only 1% to populate $7 \, ^1D_2$ (73%) or $7 \, ^1S_0$ (25%) SESs by the fluorescence decay [10].

To interpret the experimental results in Figs. 9(b) and 9(c) the contribution of the $7 \, ^1S_0$ state is neglected because the corresponding level is quite separated from the other states and the state interacts weakly with the rest of the manifold. The photoexcitation of the ith level in the $n = 7$ SES manifold

TABLE I. Calculated zero-field lifetimes of the $1s7l \, ^1L_L$ and $1s7l \, ^3L_J$ states of helium.

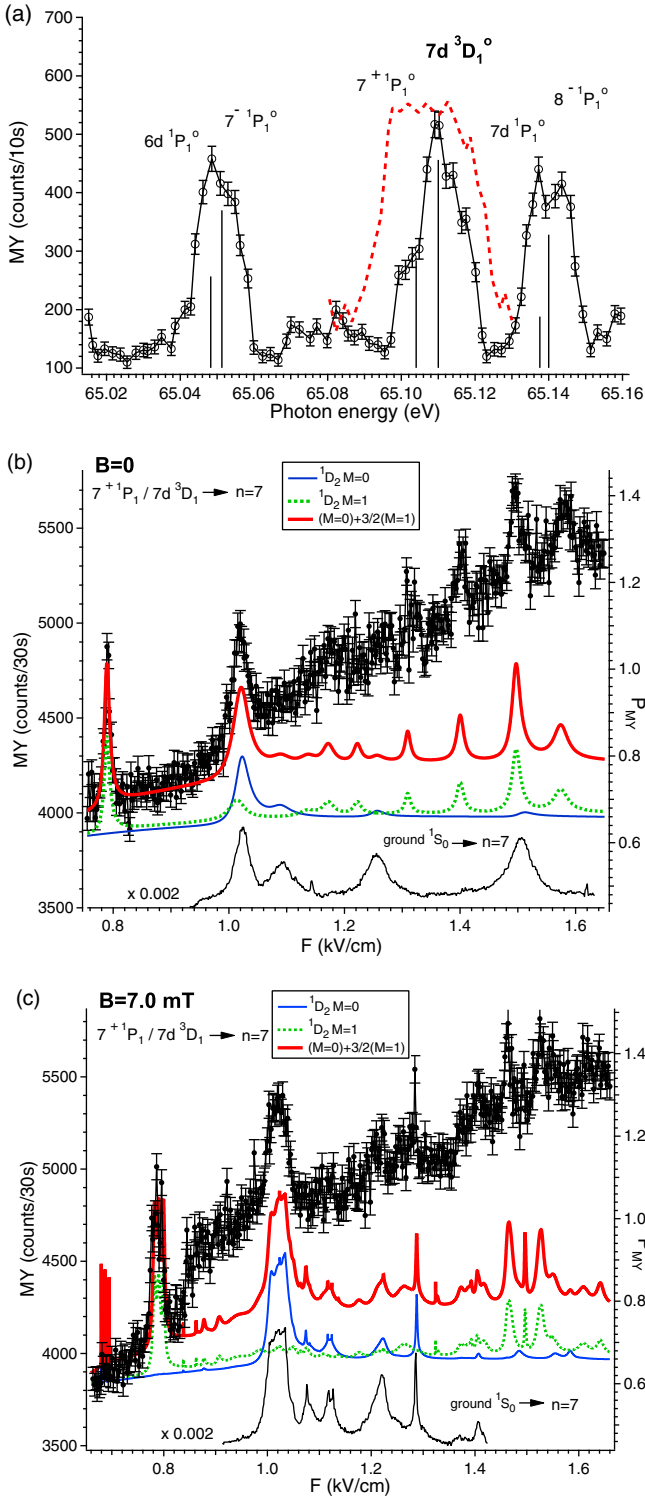| τ (ns)	^1S	^1P	^1D	^1F	^1G	^1H	^1I	^3S	^3P	^3D	^3F	^3G	^3H	^3I
	352	20.6	193	375	635	960	1351	277	514	162	375	635	960	1351

FIG. 9. (a) The MY dependence on photon energy for $F = 0$ in the region of the $n = 7$ DES for two different beamline slit settings [30 μm and 100 μm (solid line), 30 μm and 200 μm (dashed line)]. Bars denote calculated energy positions [10] and the expected MY from DESs [24]. Also shown is the measured MY and modeled P_{MY} trends as a function of F when the $n = 7$ SES manifold is populated by radiative decay of photoexcited $7^+ \, ^1P_1$ and $7d \, ^3D_1$ DESs for (b) $B = 0$ and (c) $B = 7$ mT. The M-specific P_{MY} curves are offset for 0.35.

therefore primarily depends on w^i_{1D2} and $w^i_{3D1,2}$, the weights of the $^1D_2$ and $^3D_{1,2}$ states, respectively. In the absence of full calculations including the DES manifold we proceed to estimate MY originating from the selected DESs as a function of the electric and magnetic fields. According to the multiplet weight model, the TMY and SMY created by fluorescence decay of the selected DESs are approximated by

$$\text{TMY} = A \sum_i \left(w^i_{1D2} + \kappa w^i_{3D1,2} \right) w^i_{3LJ},$$

$$\text{SMY} = A\nu \sum_i w^i_{1D2} w^i_{1LJ};$$

$$\text{TMY} = A\kappa \sum_i w^i_{3D1,2} w^i_{3LJ},$$

$$\text{SMY} = A\nu \sum_i \left(\kappa w^i_{1D2} + w^i_{3D1,2} \right) w^i_{1LJ}$$

for $7^+ \, ^1P_1$ and $7d \, ^3D_1$, respectively, where A is a common factor, depending on the experimental conditions and photoabsorption probability of the $7^+ \, ^1P_1$ state. It is assumed that only SES multiplet weights depend on the field parameters. This is a reasonable approximation because, contrary to the $n = 7$ SES, Stark mixing of the $n = 7$ DES manifold below the $N = 2$ ionization threshold is negligibly small for dc electric-field strengths of the order of 1 kV/cm [23]. Since $\eta, \kappa \ll 1$, a dominant contribution to MY is given by $\text{TMY} = A \sum_i w^i_{1D2} w^i_{3LJ}$. It may be counterintuitive that the $7^+ \, ^1P_1^o$ state is a main source of (T)MY in the investigated range because at $F = 0$ the $7d \, ^3D_1^o$ state contributes to MY twice as much [Fig. 9(a)]. However, despite relatively weak SO interaction in the zero field, it turns out that the $^1D_2$ state at 1 kV/cm is already strongly mixed with the other singlet and triplet states, making the corresponding SESs efficient TMY sources. Then the decisive factor for MY production is the magnitude of the dipole-allowed $^1P_1$ component in DESs, which is much larger for the $7^+ \, ^1P_1$ state. This view is confirmed by MY data collected for an almost pure singlet pair of DESs, $7d \, ^1P_1^o$ and $8^- \, ^1P_1^o$, photoexcited by 65.14-eV photons [Fig. 9(a)]. The measured F dependence of MY for these two states (not presented here) is practically the same as the MY data in Figs. 9(b) and 9(c).

Finally, according to the Wigner-Eckart theorem, the $M = 0$ and $M = \pm 1$ components of the $^1D_2$ multiplet are populated from the upper $^1P_1 (M = 0)$ DES with a 4:3 probability ratio. The perturbation of axial symmetry due to the presence of a 7-mT magnetic field in the perpendicular direction is weak, as shown by the small (less than 10^{-3}) relative difference of multiplet weights for $M = \pm 1$ states. The probability for the $7^+ \, ^1P_1$ DES to end in the metastable states is then estimated by

$$\text{P}_{MY} \approx \sum_i [w^i_{1D2}(M = 0) + \tfrac{3}{2} w^i_{1D1}(M = 1)] w^i_{3LJ}, \quad (14)$$

where the summation goes over all quantum states in the $n = 7$ SES manifold. This result is different than in the direct photoexcitation case because here the $^1D_2$ multiplet is activated

instead of $^1P_1$ and two types of weights must be considered, taking part in two different sets of anticrossings, namely, the $M = 0$ and $|M| = 1$ set. Figures 9(b) and 9(c) show good agreement between measured MY and estimation (14) of the multiplet weight model. Contrary to the direct photoexcitation case [Fig. 7(c)], here the model result underestimates the observed increase of MY with F. By examining the lifetimes given in Table I, one realizes that a steady increase of the ^3D multiplet weight relative to the ^1D weight would direct more decay paths to the triplet channel than predicted by the multiplet weight model, because the ^3D lifetime (162 ns) is shorter than the ^1D lifetime (193 ns). This is just opposite to the $^{1,3}P$ situation, described above. So far, this is the only indication of a DE- specific SO mixing in the AS signal.

V. CONCLUSION

The MY signal from singly excited He atoms provides an extremely sensitive test of intramanifold singlet-triplet coupling steered by external electric and magnetic fields. As shown for $n = 7$, the signal crucially depends on the way the SES manifold is populated. Namely, for each magnitude $|M|$ of the projection of the total angular momentum in a given magnetic field (only weakly perturbing the axial symmetry) a specific set of anticrossings occurs, which is a function of the applied electric-field strength. It is then evident that a different response is expected when the SES manifold is directly photoexcited from the ground state activating levels with nonzero $^1P_1(M = 0)$ weight or when it is populated by radiative decay of upper states such as those in the $n = 7$ DES manifold below the second ionization threshold. The direct photoexcitation case was studied theoretically in detail by precisely calculating SESs and their energies in the combined F and B fields and by taking into account a variety of radiation cascade paths to the final metastable states. The calculated MY map agrees very well with the experimental result. A great deal of attention was devoted to understanding why in the particular excitation mode some of the anticrossings contribute more to MY than the others. This was explained by the multiplet weight model according to which the anticrossings behave like AND gates: The population is transferred most efficiently when one arm is strongly activated by the excitation process

[the corresponding level has a large $^1P_1(M = 0)$ weight] and the other arm is strongly routed to the detection channel (the corresponding level has a large triplet weight). For a given anticrossing both conditions are fulfilled to the largest extent at field coordinates of the crossing's center. Away from the center, the population transfer mediated by the two levels may still exist, but is weaker.

It is clear that the model based only on multiplet weight products cannot precisely describe the MY trend because it neglects the variation of the decay branching ratio to the singlet and triplet metastable states, as well as the pronounced interference effects in the anticrossing region. Still, the model is able to point out the anticrossings that contribute the most to the MY signal. The concept was found useful in identifying the AS signal structure when the $n = 7$ SES manifold was excited indirectly, by the fluorescence decay of $7^+\,^1P_1$ and $7d\,^3D_1$ DESs. As expected from previously reported DES fluorescence decay rates [24], the present results confirm the activation of $^1D_2(M = 0, \pm 1)$ states within the SES manifold. The triplet counterpart states $^3D_{1,2}$ are found to play only a minor role due to a much weaker photoexcitation of the predominantly triplet DES. Apart from a steady increase of the MY, no unknown structure in the MY signal was detected that would indicate the existence of anticrossings in the examined part of the $n = 7$ DES manifold. For these to show up, much higher electric- and magnetic-field strengths would be required than used in this study [15,20,21]. To be sure about the origin, one would need to exclude anticrossings due to the intermanifold mixing of SESs, also expected to occur at high-field strengths. These SES-specific anticrossings are expected to generate a much stronger AS signal than DES-specific anticrossings. However, relying on the presented theoretical framework, it is likely that the former contribution can be subtracted from the signal.

[1] R. Panock, R. R. Freeman, B. R. Zegarski, and T. A. Miller, Phys. Rev. A **25**, 869 (1982).

[2] I. Ozier and W. L. Meerts, Phys. Rev. Lett. **40**, 226 (1978).

[3] F. Penent, D. Delande, and J. C. Gay, Phys. Rev. A **37**, 4707 (1988).

[4] E. A. Hessels, P. W. Arcuni, F. J. Deck, and S. R. Lundeen, Phys. Rev. A **46**, 2622 (1992).

[5] R. C. Stoneman, G. Janik, and T. F. Gallagher, Phys. Rev. A **34**, 2952 (1986).

[6] A. Mihelič, M. Žitnik, K. Bučar, L. Avaldi, and R. Richter, Phys. Rev. A **89**, 063422 (2014).

[7] J.-E. Rubensson, A. Moise, A. Mihelič, K. Bučar, M. Žitnik, and R. Richter, Phys. Rev. A **81**, 062510 (2010).

[8] C. E. Theodosiou, At. Data Nucl. Data Tables **36**, 97 (1987).

[9] M. Žitnik, A. Stanič, K. Bučar, J. G. Lambourne, F. Penent, R. I. Hall, and P. Lablanquie, J. Phys. B **36**, 4175 (2003).

[10] J. Söderström, M. Agåker, A. Zimina, R. Feifel, S. Eisebitt, R. Follath, G. Reichardt, O. Schwarzkopf, W. Eberhardt, A. Mihelič, M. Žitnik, and J.-E. Rubensson, Phys. Rev. A **77**, 012513 (2008).

[11] F. Penent, P. Lablanquie, R. I. Hall, M. Žitnik, K. Bučar, S. Stranges, R. Richter, M. Alagia, P. Hammond, and J. G. Lambourne, Phys. Rev. Lett. **86**, 2758 (2001).

[12] R. S. Van Dyck, C. E. Johnson, and H. A. Shugart, Phys. Rev. A **4**, 1327 (1971).

[13] S. S. Hodgman, R. G. Dall, L. J. Byron, K. G. H. Baldwin, S. J. Buckman, and A. G. Truscott, Phys. Rev. Lett. **103**, 053002 (2009).

[14] D. C. Morton, Q. Wu, and G. W. F. Drake, Can. J. Phys. **84**, 83 (2006).

[15] A. Mihelič, Fluorescence of doubly excited states of helium in homogeneous electric field, Ph.D. thesis, Univer-

sity of Ljubljana, 2006, http://www.rcp.ijs.si/amihelic/phd/thesis.pdf.

[16] G. W. F. Drake, in *Handbook of Atomic, Molecular, and Optical Physics*, edited by G. W. F. Drake (Springer, Berlin, 2006), Chap. B.11, pp. 199–219.

[17] H. Wieder and T. G. Eck, Phys. Rev. **153**, 103 (1967).

[18] R. C. Stoneman and T. F. Gallagher, Phys. Rev. Lett. **55**, 2567 (1985).

[19] J. R. Harries, J. P. Sullivan, J. B. Sternberg, S. Obara, T. Suzuki, P. Hammond, J. Bozek, N. Berrah, M. Halka, and Y. Azuma, Phys. Rev. Lett. **90**, 133002 (2003).

[20] C. Såthe, M. Ström, M. Agåker, J. Söderström, J.-E. Rubensson, R. Richter, M. Alagia, S. Stranges, T. W. Gorczyca, and F. Robicheaux, Phys. Rev. Lett. **96**, 043002 (2006).

[21] M. Ström, C. Såthe, M. Agåker, J. Söderström, J.-E. Rubensson, S. Stranges, R. Richter, M. Alagia, T. W. Gorczyca, and F. Robicheaux, Phys. Rev. Lett. **97**, 253002 (2006).

[22] K. C. Prince, M. Coreno, R. Richter, M. de Simone, V. Feyer, A. Kivimäki, A. Mihelič, and M. Žitnik, Phys. Rev. Lett. **96**, 093001 (2006).

[23] A. Mihelič and M. Žitnik, Phys. Rev. Lett. **98**, 243002 (2007).

[24] M. Žitnik, K. Bučar, M. Štuhec, F. Penent, R. I. Hall, and P. Lablanquie, Phys. Rev. A **65**, 032520 (2002).